Magn Reson Mater Phy (2013) 26:477–490
DOI 10.1007/s10334-013-0372-9

RESEARCH ARTICLE

Alleviating artifacts in ^{1}H MRI thermometry by single scan spatiotemporal encoding

Rita Schmidt · Lucio Frydman

Received: 21 August 2012 / Revised: 17 January 2013 / Accepted: 4 February 2013 / Published online: 27 February 2013

Abstract
Objective Recent years have seen an increased interest in combining MRI thermometry with devices capable of destroying malignancies by heat ablation. Expected from the MR protocols are accurate and fast thermal characterizations, providing real time feedback on restricted tissue volumes and/or rapidly moving organs like liver. This article explores the potential advantages of relying on spatiotemporally encoded (SPEN) sequences for retrieving real-time thermometric images based on the water's proton resonance frequency (PRF) shifts.
Materials and methods Hybrid spatiotemporal/*k*-space encoding single-scan MRI experiments were implemented on animal and human scanners, and their abilities to deliver single- and multi-slice real-time thermometric measurements based on PRF-derived phase maps in phantoms and in vivo, were compared against echo planar imaging (EPI) and gradient-echo counterparts.
Results Under comparable acquisition conditions, SPEN exhibited advantages vis-à-vis EPI in terms of dealing with inhomogeneous magnetic field distortions, with shifts arising due to changes in the central frequency offsets, with PRF distributions, and for zooming into restricted fields-of-view without special pulse sequence provisions.
Conclusion This work confirms the ability of SPEN sequences, particularly when implemented under fully-refocused conditions, to exploit their built-in robustness to shift- and field-derived inhomogeneities for monitoring thermal changes in real-time under in vitro and in vivo conditions.

Keywords Spatiotemporal encoding · Real-time MRI · ^{1}H-based thermometry · In vivo PRF · Restricted FOV

Abbreviations

MRI	Magnetic resonance imaging
NMR	Nuclear magnetic resonance
FOV	Field of view
FT	Fourier transform
SPEN	SPatio-temporal ENcoding
PRF	Proton resonance frequency
STD	Standard deviation
SNR	Signal-to-noise ratio
SR	Super-resolution
SAR	Specific absorption rate
RF	Radio frequency
RO	Readout
PE	Phase-encode
SS	Slice-select
TE	Echo time
TR	Repetition time
EPI	Echo-planar imaging

Introduction

Among its many contemporary applications, "ultrafast" MRI is used for obtaining real-time information on temperatures changes undergone by tissues under in vivo

Electronic supplementary material The online version of this article (doi:10.1007/s10334-013-0372-9) contains supplementary material, which is available to authorized users.

R. Schmidt · L. Frydman (✉)
Chemical Physics Department, Weizmann Institute of Science, 76100 Rehovot, Israel
e-mail: lucio.frydman@weizmann.ac.il

conditions. These "MR thermography" measurements rely on water's well-documented −0.01 ppm/°C chemical shift temperature dependence [1–3]. If suitably characterized and combined with imaging modalities, these proton resonance frequency (PRF) shifts can be exploited in different therapies, including guiding laser- and ultrasound-focused ablation [1–5]. Some forms of MR thermography include direct measurements of water's chemical shift by spectroscopic imaging, either in a reference-less mode or in combination with other tissue resonances acting as internal references [6, 7]. Another approach to determine PRFs is by monitoring the phase shift changes that water's temperature-dependent shifts will impart on different voxels upon introducing a single delay prior to an image's acquisition. All these applications require that the voxels themselves be imaged using rapid techniques, so as to provide a real-time feedback mechanism for guiding the invasive treatment/device. Such rapid imaging characterizations have been primarily based on echo-planar imaging (EPI) [8, 9], and have led to considerable successes in MRI-integrated tumor ablation treatments. This endeavor, however, is not without its challenges. Single-shot PRF measurements based on EPI face a number of complications arising from organs which are motion-prone like livers or kidneys, due to the method's need for high spatial resolutions–which often calls for restricted Fields-of-View (FOVs), and due to a need to target areas subject to sizable magnetic field inhomogeneities including those close to the intestines (e.g., uterine fibroids), abdomen, or lungs. Also worth noting are the challenges that frequency offsets arising from either treatment devices placed in close proximity to the regions of interest, from high fat contents that may cause an incorrect central frequency selection, or even due to the effects that the heating process itself, will impart on the water resonance. When relying on MRI as the feedback mechanism for a treatment or device, all such shifts can disrupt the accurate targeting of a region and/or treatment of the lesion – particularly in high-B_0 magnets. Still, given the promises carried by these real-time procedures, a number of solutions have been put forward to compensate for these weaknesses. These include the restriction of EPI's FOV with the assistance of parallel imaging and/or multidimensional RF pulses [10, 11], the use of multi-shot and/or multi-segment EPI procedures [12–15], the reliance on independently derived field maps of ΔB_o inhomogeneities, or the use of other sequences such as rapid multi-scan gradient echo to satisfy the fast imaging requirements [9]. The present work explores the options that in this area are opened by yet another alternative capable of delivering the images sought within single shot, but which instead of k-space encoding relies on spatiotemporal manipulations for performing the MRI.

While initial developments in manipulations that excite and collect spin signals sequentially in both space and time were explored decades ago [16, 17], recent years have witnessed a revived interest in such procedures. A main driving force for this stemmed from the realization that spatiotemporal encoding (SPEN) enables the acquisition of arbitrary multidimensional NMR spectra within a single scan [18]. Recent publications have explored and demonstrated that such sequences can also be advantageously exploited in purely imaging-oriented single scan multidimensional acquisitions [19–23]. Particular advantages result when relying on "Hybrid" schemes [19, 20] whereby the robust, high-bandwidth readout direction of a 2D MRI acquisition is encoded in k-space, and SPEN is exploited to unravel the more artifact-prone, low-bandwidth direction. Besides a higher intrinsic immunity to ΔB_0 inhomogeneities, this approach offers the capability of performing "fully-refocused" scans, whereby each instant throughout the data acquisition process corresponds to the formation of a spin-echo from the signal-contributing voxels [20]. Yet another built-in advantage of SPEN stems from its avoidance of a numerical Fourier transform (FT); this allows one to restrict FOVs without experiencing image folding, and without interferences arising from the presence of multiple chemical shifts. In their original implementations, SPEN imaging techniques suffered from a number of drawbacks vis-à-vis EPI; particularly lower spatial resolutions, higher specific absorption rate (SAR) values, and limitations in the rapid acquisition of multi-sliced 3D imaging information. Recent publications, however, have opened up ways to deal with these drawbacks by means of super-resolution (SR) and adiabatic passage methods [24–27], which make SPEN-based techniques alternatives worth exploring when facing challenging applications [22, 25]. In view of all these features, this article explores the potential of SPEN for thermometry purposes. As further detailed below, comparable thermal measurements can be extracted from this technique as from EPI-based counterparts under ideal conditions. A number of implementations based on both fully-refocused and non-fully-refocused sequences highlight the superior performance that SPEN techniques yield when dealing with more challenging scenarios–including those currently restricting certain thermometric applications.

Materials and methods

SPEN-based single-scan 2D MRI: principles and sequencing considerations

Before focusing on the relative merits of SPEN's thermometric applications, it is convenient to briefly summarize

how SPEN delivers its single-scan imaging information and its differences vis-à-vis EPI. This is simplest to visualize first in a 1D experiment, assumed to focus on retrieving a y–axis profile. The SPEN will rely on a chirp radiofrequency (RF) excitation pulse acting during a time T_{exc} in combination with a gradient G_{exc}, to introduce a spatially-dependent parabolic phase profile:

$$\phi_{exc}(y) = -\frac{\gamma G_{exc} T_{exc}}{2FOV} y^2 + \frac{\gamma G_{exc} T_{exc}}{2} y + \text{const}, \quad (1)$$

where the range of the sweep γG_{exc}FOV defines the targeted field-of-view (FOV). This encoding is followed by a readout, whereby an acquisition gradient $G_{acq}(t)$ acts over a time T_{acq} such that $k_{acq}(t = T_{acq}) = \gamma \int_0^{T_{acq}} G_{acq}(t)dt = -G_{exc}T_{exc}$ (i.e., $G_{exc}T_{exc} = -G_{acq}T_{acq}$ for a constant G_{acq}). Relying on a Stationary Phase Approximation [18]

$$\frac{d}{dy}\{\phi_{exc}(y) + k_{acq}(t) \cdot y\}_{y=y_{SPA}(t)} = 0, \quad (2)$$

whereby spin-packets interfere destructively everywhere in the sample except in the point y_{SPA} (in whose neighborhood the spins' evolution phases have a "flat" profile), it follows that the acquired time-domain signal $S(t)$ will reflect in its magnitude the spin's density profile along the FOV range, according to

$$|S(t)| \propto \Delta y \cdot \rho(y_{SPA(t)}). \quad (3)$$

Here Δy is a nominal spatial resolution defined during the encoding by the parabolic phase's curvature $\Delta y = \sqrt{\frac{FOV}{\gamma G_{exc} T_{exc}}}$. Recent publications have discussed a variety of single-shot alternatives for acquiring 2D and multi-slice 3D images based on this strategy [18–23]; as mentioned, here we shall concentrate on "Hybrid" approaches encoding the read-out direction in a usual *k*-space fashion, while using SPEN to rasterize the image in what would normally be a "low bandwidth" dimension.

Figure 1 compares the Hybrid SPEN sequences assayed in this work, with a spin-echo EPI counterpart. Notice that despite the analogous acquisition structures of the Hybrid and EPI sequences, the latter requires an FT to deliver its phase-encoded imaging information, whereas SPEN's blipped dimension provides its information in direct image space. Two versions of SPEN-based hybrid imaging sequences are treated here. One imparts its encoding by a 90° chirp RF excitation of the whole sample followed by a slice-selective (SS) refocusing of the region to be targeted (Fig. 1b); a second variant is based on a 90° slice-selective excitation and pairs of 180° RF pulses (Fig. 1c). The latter's usefulness results from its compatibility with multi-slice acquisitions on 3D volumes. Notice that given this sequence's reliance on a broadband 180° adiabatic sweep for spatial encoding of a selectively-excited slice of interest, a rewinding of the remaining magnetizations is required. This could be done using adiabatic sweeps [19, 27], but to minimize the sequence's SAR a hard, slab-selective 180° pulse was utilized instead.

An important feature of these approaches concerns their "full-refocusing" abilities [20], allowing one to achieve a particularly high immunity to ΔB_0 inhomogeneities and other offset-derived distortions. Full refocusing is a particular form of spin echo whereby the scan's timing parameters are set so as to endow individual spin-packets with a full refocusing of their T_2*/shift effects, at instants corresponding to the achievement of their respective SPAs (Eq. 2). This possibility arises due to the progressive way by which spins are excited and detected in SPEN. For the sequences that will be here used for thermal imaging, these conditions are fulfilled by setting $T_{exc} = T_{acq}$ if SPEN is imparted by a 90° chirp pulse, and by introducing a free-evolution delay $T_{acq}/2$ in case SPEN is imparted by a 180° adiabatic inversion pulse of duration $T_{180} = T_{acq}/2$ (Fig. 1b, c). In addition to benefiting from these full-refocusing conditions, SPEN's sensitivity and resolution can be further improved by departing from the simple magnitude-mode processing conveyed by Eq. (3), and upgrading it to a Super Resolution (SR) reconstruction [24]. The SR expands SPEN's formulation beyond the stationary phase approximation, and extracts imaging information from within the parabolic phase summarized by Eq. (1) by recasting Eq. (3) into a phase-sensitive formulation of the digitized signal: $S(t) = A_{SR}(t, y)\cdot\rho_{SR}(y)$. Here A_{SR} is a point-spread function matrix containing all the phase encoding and decoding information and depending on a priori known sequence parameters, and ρ_{SR} is the spin density being sought. By casting back the image-reconstruction procedure as this set of linear equations, involving the calculation of each of the image's pixels by a summation of multiple phase-corrected sampled data points, SR reinstates the multiplexing advantage that had been lost by the simple magnitude-mode image reconstruction. Moreover, by exploiting the fact that signals $S(t)$ in SPEN experiments are usually sampled at dwell times Δt that are significantly shorter than the sampling rate $\gamma G_{acq}\Delta y$ demanded by Eq. (3)'s basic resolution expectation, a significantly higher spatial definition is simultaneously achieved. The increased sensitivity and spatial resolution that the SR procedure affords, is illustrated for a standard ACR phantom in Fig. 2. In this example $\rho_{SR}(y)$ was solved by a first-iteration Conjugate Gradient (CG) solution [24]; as described in a number of literature instances [18, 24, 25], this Figure clearly demonstrates the higher resolution and sensitivity that SR imparts on the hybrid SPEN experiment, vis-à-vis a basic magnitude-mode reconstruction.

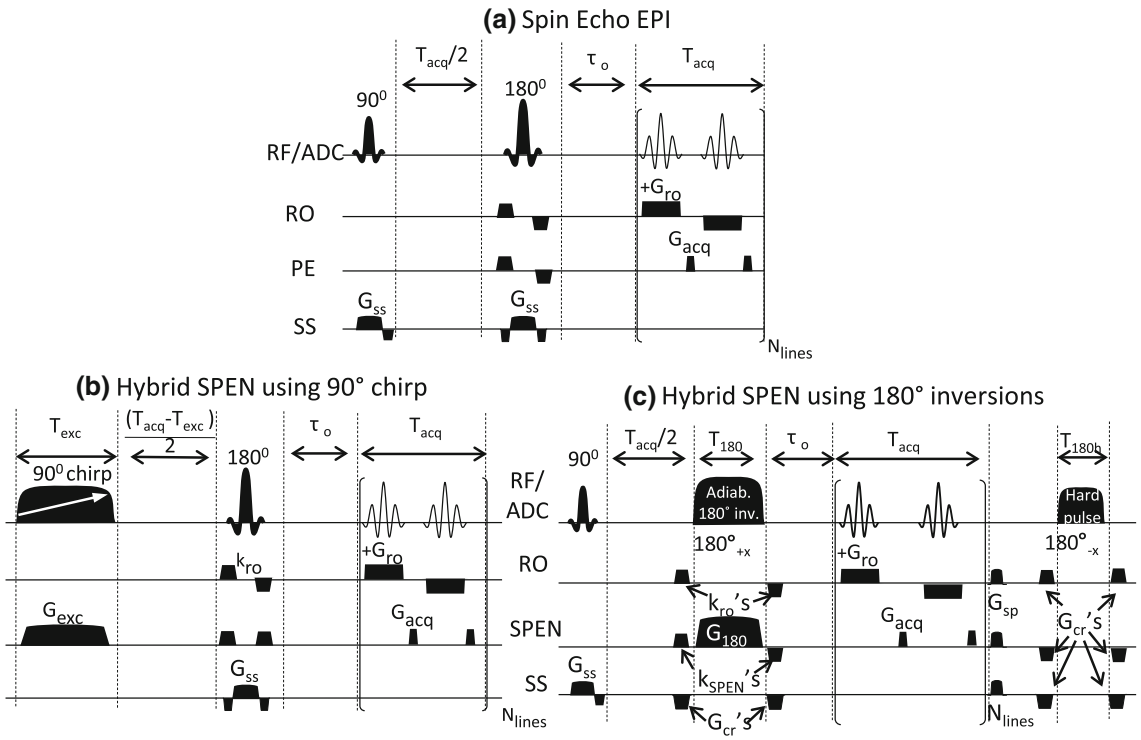

Fig. 1 Sequences used in this study: (**a**) Spin-Echo EPI. **b** Real-time Hybrid SPEN based on a 90° chirp encoding. **c** Multislice sequence employing an adiabatic 180° passage for SPEN, and a final 180° hard pulse for re-equilibrating the magnetizations of non-encoded positions. The SPEN sequences are akin to fully-refocused proposals that have been introduced and discussed in the past [18–20, 27], but incorporate **a** τ_o delay for assessing thermal changes via PRF-derived phase shifts of the imaging signals. The definition of various parameters involved include: a RF/ADC row displaying the RF pulses and the acquisitions' timing (ADC for Analogue-to-Digital Converter); RO, PE/SPEN and SS rows displaying the gradients applied along the readout, the phase- or spatiotemporally-encoded and the slice-selective directions, respectively; $T_{acq/exc}$, $G_{acq/exc}$—acquisition or excitation durations and gradient strengths associated with the PE/SPEN dimensions; T_{ro}, G_{ro}—acquisition duration and gradient strength associated with the orthogonal read-out dimension; N_{lines}—number of PE/SPEN-encoded elements; T_{180},G_{180}—180° duration and gradient strength associated with the inversion pulse; k_{ro} and k_{SPEN}—pairs of prewinding gradients flanking the adiabatic 180° inversion and imparting $\approx\gamma G_{ro}T_{ro}/4$ and $\approx\gamma G_{180}T_{180}/2$ encodings, respectively. All slice-selective and 180° pulses are flanked by crusher or shifting gradients, as needed. Further details on the SPEN sequences are given in section "Materials and methods", and the values of all relevant parameters used for the various experiments are further specified in the corresponding captions

Resolution is in fact comparable to the FOV_y/N_{acq} values associated an ideal EPI scan, where N_{acq} is also the number of points used in the SR reconstruction. For all the cases reported below the spatial resolutions quoted along the SPEN dimensions reflect these SR-endowed gains. Also sensitivities end up, on average and when dealing with homogeneous environments, similar for SE EPI and for fully-refocused SPEN experiments. At the same time, SR helps one to reduce SPEN's usually higher SAR percentages and without impairing SPEN's robustness to sampling- or shift-derived imperfections.

Real-time SPEN MRI: thermometric considerations

In order to extract PRF values from single-scan SPEN images—and from there temperature changes ΔT—we focused on the phase shifts arising upon introducing τ_o delays into the original sequences, as indicated in Fig. 1. The $\Delta\varphi$ phase shifts experienced by each pixel in the image can be then expressed as $\Delta T = \frac{\Delta\varphi}{\alpha\cdot\gamma B_o\cdot\tau}$ [24], where $\alpha = -0.01$ ppm/°C is the PRF thermal change coefficient and γB_o defines the Larmor frequency. In EPI, the frequency-encoding τ delay is uniform for all positions. In SPEN one needs to distinguish among two cases. In fully refocused experiments [20], which often yield the highest quality images, the addition of a τ_o delay prior to the data acquisition (Fig. 1b, c) "breaks" to some extent the aforementioned full-refocusing demands. Still, as τ_o values are generally small vis-à-vis T_{acq}, this effect will be small and will affect all the spatially-encoded positions equally. By contrast, if non-fully-refocused conditions $T_{exc} < T_{acq}$ or $T_{180} < T_{acq}/2$ are chosen for Fig. 1b, c, respectively, the

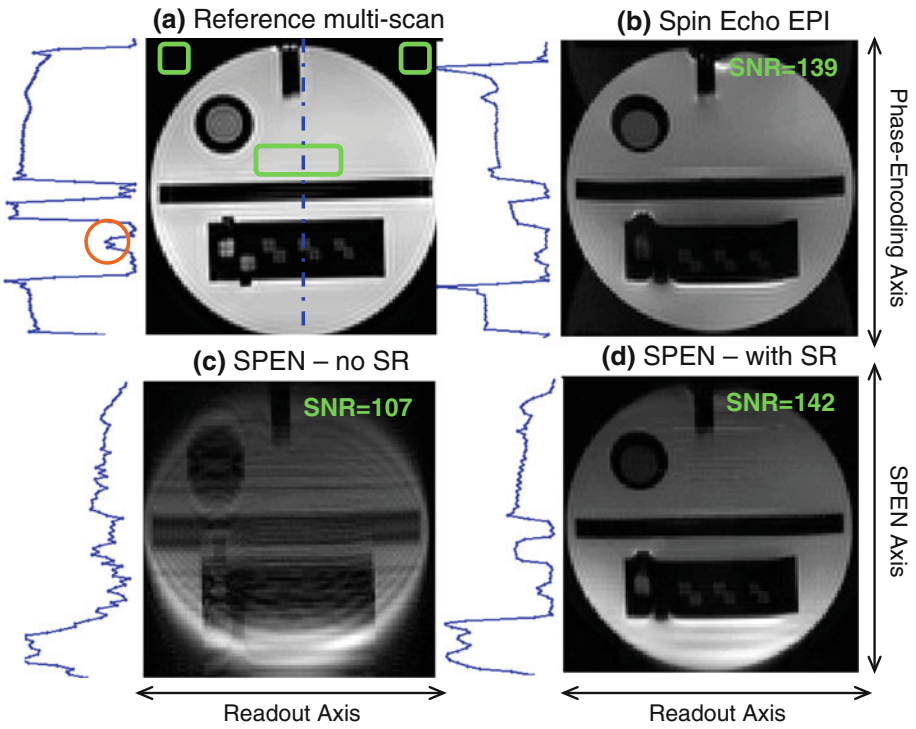

Fig. 2 Resolution and SNR improvements brought about when imparting the SR procedure on SPEN images. All data were collected at 3 T on a Siemens scanner on an ACR Accreditation Program Phantom normally used for resolution tests, aiming to resolve the 2 mm patterns appearing in the center of the lower arrays (one of which is marked by an orange circle in the reference scan). Shown alongside each 2D image are profiles corresponding to the phase-encoded/SPEN axes extracted at the position of the dashed blue line; also shown are the SNR values arising from dividing the integrated signals for the region indicated by a *green rectangle*, by the average noise in the regions indicated by the *upper smaller squares*. **a** Reference multi-scan image, (**b**) single-scan spin echo EPI, (**c**, **d**) single-scan Hybrid SPEN images (sequence in Fig. 1b). reconstructed using a simple magnitude calculation or a Super Resolution approach. The non-uniform signal intensity in the SPEN images reflects the increasing TEs associated to this sequence. Common EPI and SPEN scan parameters: slice thickness = 5 mm, FOV = 200 × 200 mm^2, resolution 2 × 2 mm^2 (100 × 100 pixels matrix), T_{acq} = 69 ms; for the SPEN sequence T_{exc} = 69 ms, and G_{exc} = 0.027 G/cm. Multi-scan parameters: slice thickness 5 mm, FOV = 256 × 256 mm^2, resolution 2 × 2 mm^2 (128 × 128 pixels matrix), TE = 75 ms, TR = 1500 ms

effective $\tau(y)$ encoding the temperature change becomes location dependent. This delay will be $\tau(y) = \tau_o + t_{acq}(y)\cdot(1 - T_{exc}/T_{acq}) - (T_{acq} - T_{exc})/2$ for the sequence in Fig. 1b—where $0 \le t_{acq}(y) \le T_{acq}$ denotes the delay for which a particular y location in the experiment was monitored as measured from the beginning of the acquisition process—and $\tau(y) = \tau_o + t_{acq}(y)\cdot(1–2T_{180}/T_{acq}) - (T_{acq}/2 - T_{180})$ for the multi-slice experiment. Since temperatures will in such instance be given by $\Delta T = \frac{\Delta\varphi}{\alpha\cdot\gamma B_o\cdot\tau(y)}$, one needs to choose a PRF-encoding delay that—in addition to regular considerations such as the temperature resolution desired—fulfills $\tau_o > |T_{acq} - T_{exc}|/2$, $|T_{acq}/2 - T_{180}|$. Another relevant point to examine concerns the temperature measurement's standard deviation (STD). This parameter will be inversely proportional to the image's signal-to-noise ratio SNR and to the τ period: $STD_{\Delta\Phi} \propto 1/(\tau\cdot SNR)$ [28]. In SPEN experiments carried out without use of full refocusing, τ's y-dependence means that the experiment's accuracy will also be position dependent.

With such considerations as background, the temperature maps reported throughout this study were calculated by relying on the experimental phase changes measured between consecutive pairs of measurements, $\Delta T_{n,n-1}(x, y) = \frac{\Delta\varphi_{n,n-1}(x,y)}{\alpha\cdot\gamma B_o\cdot\tau(y)}$. This step-by-step approach was preferred over an absolute phase shift calculation, in an effort to avoid potential phase-wrapping complications. Absolute temperature maps could still be calculated from cumulative changes by using the fact that each voxel's temperature $T(x, y)$, fulfills $T_n(x,y) = T_o(x,y) + \sum_{k\le n}\Delta T_{k,k-1}(x,y)$. For lack of reliable ways to determine in general an absolute initial reference temperature, T_0 was taken as zero. All thermal maps reported in this work therefore represent thermal changes with respect to the first scan. Still, thanks to the high reproducibility of our heating

processes (as concluded from independent external measurements as well as by gradient-echo multi-scan MRI measures) quantitative comparisons among the various imaging techniques could be carried out. High reproducibility also enabled us to compare repeat experiments, without requiring the use of thermal sensing elements inside the magnets. In both the ex and the in vivo experiments the standard deviations of our thermal measurements were calculated in a set of experiments run without heating or cooling, by subtracting the average temperature arising from the corresponding maps over an area of relevance inside the object, and evaluating the ensuing dispersion.

Experimental setups

The feasibility and advantages associated with SPEN-based thermometry were examined on two platforms, on which all sequences in Fig. 1 were implemented. These measurements involved either a 3 T Siemens TIM TRIO clinical system using a 4-grouped channels TIM^{TM} head coil with FOVs of $300 \times 300 \times 330$ mm^3, or a 7 T Varian VNMRS vertical microimaging system using a quadrature-coil Millipede® probe with FOVs of $30 \times 30 \times 46$ mm^3. In all cases but for the EPI-based Siemens experiments, for which system-supplied sequences were used—pulse sequences were custom written with RF pulses and gradient shapes designed in MATLAB® (The MathWorks, Inc., Natick, MA) and uploaded onto the scanners; these are all available upon request. All sequence parameters were individually optimized for their thermometry applications. Images were reconstructed using custom-written MATLAB packages, which included the possibility to process hybrid data with SR along the SPEN axis and FT along the *k*-dimension [23]. 2D FT scripts for processing reference EPI and multi-scan gradient-echo phase encoded spin-warp images, were also written. Manipulations in these data processing algorithms included the alignment of positive and negative readout echoes (for EPI), weighting, etc.; as well as determinations of the voxel's changes in phase.

A summary of the experiments implemented in these platforms is given in Table 1. Single-slice tests were conducted at 7 T. These measured the temperature of water in tubes that were heated to 75 ± 1 °C, inserted into the MRI, and scanned while they cooled down. The τ_0 delay used for monitoring these thermal changes was 9 ms and the recycle time TR of the experiments was 10 s—a relatively long delay, but suited to the slow water cooling processes that were monitored. Variable-temperature measurements in tissues under both ex- and in vivo conditions were also carried out on this 7 T vertical system. To this effect temperatures were dialed into an FTS® gas-cooler/heater capable of reaching ±80 °C; an air gas stream passing through this system was delivered to the specimens by plastic tubes, and ca. ±7 °C departures from room temperature could be implemented in this fashion. Following their initial ex vivo validation, these tests were conducted on mice; these in vivo experiments, as well as all associated animal handling procedures, were done in accordance with protocols approved by the Weizmann Institute's Animal Care and Use Committee. In these experiments the animal was anesthetized and cool/warm gas fed into a thin quartz tube (to increase the thermal conductivity) attached to the animals thigh. Prior to the experiments, tuning and local shimming were performed, and the animal breathing was stabilized to minimize motional influences on the measurements. The TR between EPI and hybrid SPEN acquisitions was set to 2 s; these scans were collected in an interleaved fashion, and were started when the respiration monitoring system showed that breathing had reached a steady state. The overall sequence's duration was 22 min, with the temperature change starting after the first 10 min.

Multi-slice verification experiments were implemented on a 3 T clinical scanner. In these thermal tests a Siemens-provided gradient echo EPI and the SPEN sequence in Fig. 1c were repeated in an alternate manner, while monitoring the cooling process of a pre-heated water tube inserted in a room temperature water flask. This led to a rapid cooling of the former and to a concomitant heating of the latter. In these thermal MRI scans each set of multi-slice experiments involved 15 measurements; each of these was then repeated in an alternating EPI/SPEN/EPI/SPEN… format, until the cooling of the inner tube was completed. Such alternating execution of EPI and SPEN allowed us to verify the agreement between these thermal measurements; as described earlier, the phase observed for each voxel in the first image of each set defined the thermal reference for all subsequent scans in this set. Both sequences used similar timings and delays, with $\tau_o = 19$ ms in the SPEN sequence and TE = 19 ms in the gradient echo EPI one. For all these cases, TR = 6 s, which was fast enough to monitor the relatively slow cooling/heating processes here recorded. Also worth noting are the SAR of the different sequences that were assayed; according to the 3 T scanner's calculations, SAR percentages under the parameters assayed were ≈ 3 % for the gradient echo EPI sequence, ~ 5 % for spin echo EPI, ~ 8 % for the single-slice SPEN sequence in Fig. 1b, and ~ 15 % and for multi-slice SPEN in Fig. 1c.

Table 1 Summary of the experimental aims, platforms, sequences compared, targeted systems and scanning parameters, for the various tests assayed in this study

Experimental aims	MRI system	Sequences employed	Investigated system	Scanning parameters	Results
General comparison, slice-selective thermal sequences	7 T	Gradient echo multi-scan, spin echo EPI (Fig. 1a), single-slice Hybrid SPEN (Fig. 1b)	Cooling water tube	For the multi-scan sequence: FOV = 30 × 30 mm^2, 128 × 128 pixels matrix, 1 mm slice thickness, TR = 80 ms, full acquisition time 10 s. Common EPI and SPEN parameters: FOV of 25 × 25 mm^2, slice thicknesses of 1 mm, 70 × 70 pixels matrix, T_{acq} = 21 ms, G_{exc} = 0.5 G/cm for SPEN, TE = 9 ms for EPI, τ_o = 9 ms, TR = 10 s	Fig. 3
Fully- and non-fully-refocused SPEN comparison	7 T	Single-slice hybrid SPEN (Fig. 1b): fully and non-fully-refocused conditions	Cooling water tube	Common acquisition parameters: 30 × 30 mm^2 FOVs, 1 mm slice thickness, 70 × 70 pixels matrix, G_{acq} = 0.5 G/cm, TR = 10 s, τ_o = 9 ms, total duration of 50 ms. The fully-refocused 90° chirped SPEN used T_{exc} = T_{acq} = 21 ms, G_{exc} = 0.5 G/cm, image acquisition in 56 ms; the non-fully-refocused SPEN acquisition used T_{exc} = 4 ms, T_{acq} = 21 ms, G_{exc} = 2.1 G/cm	Fig. 4
Multi-slice comparisons in a clinical scanner	3 T	Multi-slice gradient Echo EPI and Hybrid SPEN (Fig. 1c)	Cooling/heating water flasks	Common acquisition parameters: slice thickness = 3 mm; FOV = 200 × 200 mm^2, 64 × 64 pixels matrix, TR = 6 s. SPEN-specific parameters: T_{acq} = 29.4 ms; T_{180} = 14.8 ms and G_{180} = 0.47 G/cm, τ_o = 19 ms in SPEN and TE = 19 ms for EPI	Fig. 5
Water's spatial miss-registration due to thermal changes	7 T	Spin Echo EPI (Fig. 1a), single-slice Hybrid SPEN (Fig. 1b)	Spatial offset observed upon cooling water	Common scan parameters: Slice thickness 2 mm, FOV = 25 × 25 mm^2,70 × 70 pixels matrix, τ_o = 9 ms, T_{acq} = 31 ms; for the SPEN sequence T_{exc} = 26 ms, and G_{exc} = 0.95 G/cm	Fig. 6a
Overall sensitivity to chemical shift offset	3 T	Spin Echo EPI (Fig. 1a), Hybrid SPEN (Fig. 1b)	Water tube: On- and off-resonance effects	Slice thickness 5 mm, FOV = 200 × 200 mm^2, 64 × 64 pixels matrix, echo spacing = 0.46 ms, T_{acq} = 30 ms, τ_o = 19 ms. For the SPEN experiment T_{exc} = 30 ms, G_{exc} = 0.08 G/cm	Fig. 6b
Monitoring SPEN's zooming abilities	7 T	Spin Echo EPI (Fig. 1a), Hybrid SPEN (Fig. 1b)	Cooling and heating water tubes	For all images: slice thickness = 2 mm; FOVs = 25 × 25 mm^2; 70 × 70 pixels matrix, TR = 10 s and half-FOVs refer to half these magnitudes along the SPEN axis. In all experiments T_{acq} = 30.8 ms, τ_o = 5 ms; for the SPEN sequence T_{exc} = 26 ms and G_{exc} = 0.95 G/cm	Fig. 7
SPEN's in vivo thermal abilities	7 T	Spin Echo EPI (Fig. 1a), Hybrid SPEN (Fig. 1b)	Mouse: temperature profiles in muscle area	Common scan parameters: τ_o = 4 ms, slice thickness 1 mm, FOVs = 30 × 30 mm^2, 35 × 70 pixels matrix, TR = 2 s. For SPEN: T_{exc} = T_{acq} = 21 ms, G_{exc} = 0.3 G/cm	Fig. 8
SPEN's ability to cope with inhomogeneous fields	7 T	Spin Echo EPI (Fig. 1a), Hybrid SPEN (Fig. 1b)	Cooling water tube in inhomogeneous environment	Common scan parameters: τ_o = 5 ms, 25 × 25 mm^2, pixel matrix 70 × 70, T_{acq} = 30.8 ms, TR = 10 s. For the SPEN T_{exc} = 26.8 ms, G_{exc} = 0.92 G/cm	Supplementary Fig

Results

General features of SPEN-based thermometry: controlled phantom examples

Figure 3 presents water cooling comparisons resulting from monitoring phase-derived PRF shifts using gradient-echo multiscan MRI, spin-echo EPI and a fully refocused SPEN sequence based on Fig. 1b. The $T_{exc} = T_{acq}$ condition used in this acquisition means that the same $\widetilde{\tau}_o$ value characterized all positions. The Figure shows magnitude images as well as temperature map progressions that fit equally well all three methods—although, even for such a well-shimmed, controlled environment, one can already appreciate smaller distortions in the SPEN images compared to the EPI counterparts. A 4×4 mm^2 area in the center of the samples was used to quantitatively compare among the methods; small ($\leq$0.4 °C) systematic differences –which could reflect minor timing differences– are apparent; yet the matching between all measurements and their very similar STDs, are remarkable.

Another verification worth discussing concerns comparisons among Hybrid SPEN tests run in fully-refocused and non-fully-refocused modes. Figure 4 illustrates the clearly y-dependent phase shifts arising in the latter cases' raw phase maps, which only revert to the homogeneous conditions upon accounting for the $\tau(y)$-dependence alluded to in the Methods section. Also worth remarking is the fact that the same $\tau(y)/\Delta\varphi(y)$-dependence leads to a standard deviation in the temperature that varies from one edge of the image to another.

Figure 5 illustrates the compatibility of SPEN-based thermometry sequences with fast multi-slice acquisitions. Figure 5a, b display thermal-change profiles obtained with the SPEN sequence shown in Fig. 1c at 3 T against results arising upon executing Gradient-Echo EPI scans. Each EPI or SPEN set contained 15 scans repeated with a TR = 6 s, and both EPI and SPEN were executed in an interleaved manner addressing the same five slices. In this way, the temperature changes afforded by the Hybrid SPEN could be compared against EPI multi-slice counterparts. The examined phantom consisted of a hot pear-shaped water ampule, placed at ca. 80 °C inside an outer round flask with room temperature water. Accordingly, changes in the diameter of the inner container could be tracked as a function of the slice's position, while thermal variations of opposite sign could be monitored in the inner and outer containers' cross-sections. All these expectations are very well born out by the representative experiments shown in Fig. 5a, b; notice that apart from the absence of half-FOV distortions, the SPEN data compare favourably with the EPI. Shown in Fig. 5c are longer-term, comprehensive

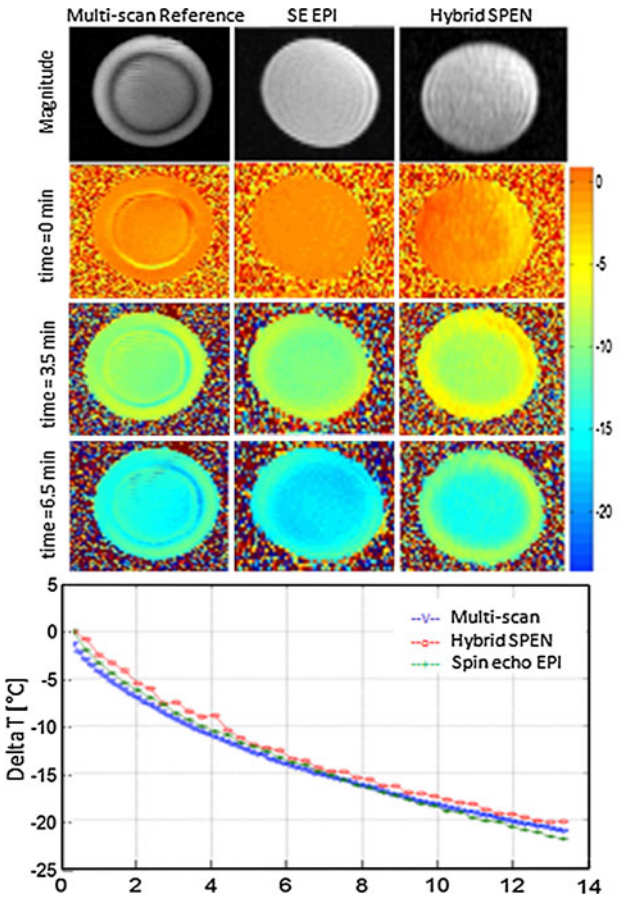

Fig. 3 Water cooling progression monitored at 7 T by a multi-scan gradient-echo reference, and by single-scan EPI and single-slice SPEN methods. In all experiments water was heated to 75 °C, a point taken as "zero temperature" in the subsequent maps. Temperature progressions are illustrated for the magnitude images displayed on top, for three cooling time points. The *color bar* to the right of these temperature progressions—like all *color bars* in the remainder of this work—denote temperature changes in units of °C. Illustrated in the bottom plot are temperature profiles arising from averaging phase shifts for a 4×4 mm^2 area in the middle of the water tube. The multi-scan sequence used a FOV of 30×30, 0.23×0.23 mm^2 resolution (128×128 pixels matrix), 1 mm slice thickness, TE/TR = 9/80 ms, full acquisition time 10 s. The EPI and 90° chirp SPEN sequences are shown in Fig. 1a, b, and used a FOV of 25×25 mm^2, slice thicknesses of 1 mm, resolutions of 0.36×0.36 mm^2 (70×70 pixels matrix), $T_{acq} = 21$ ms, $\tau_o = 9$ ms; $G_{exc} = 0.5$ G/cm for SPEN. Thermal maps are shown "unmasked" for the sake of better comparing among the methods. The origin of the artificial "temperature jump" evidenced by all images as a thin rim at the interfaces between the tubes stems from unstable phase values, possibly reflecting the onset of convectional motion

summaries of these thermal changes: these panels show overlaid temperature progressions for the five slices arising from the alternating EPI/SPEN/EPI/… series, for temperatures averaged over a 34×34 mm^2 area of the phantom's center vessel. Once again, these graphs show an excellent match between both sets of images,

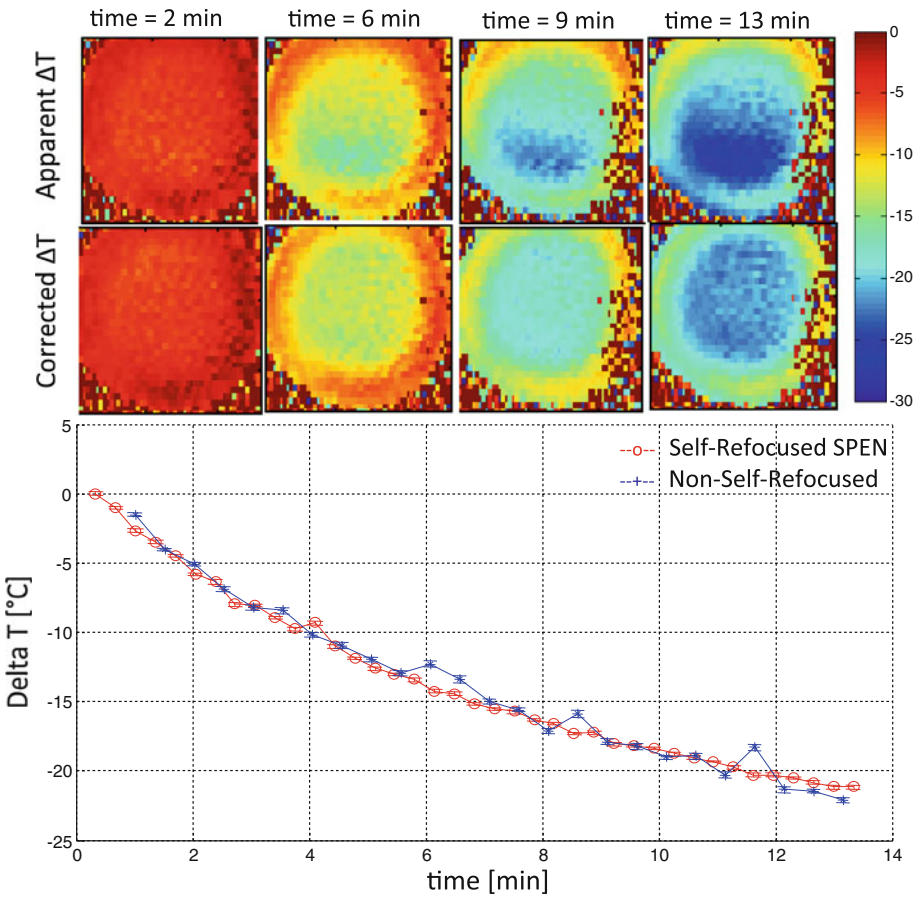

Fig. 4 Temperature maps calculated from non-fully-refocused SPEN acquisitions showing an apparent *y*-dependent ΔT, compared *vs* the corrected, uniform ΔT arising if taking into account the differing delays versus *y*-location. Temperature changes can be read from the *color bar* on the right, in °C. Compared on the bottom graph are temperature profiles based on non-fully-refocused and fully-refocused cases. Both sequences were implemented at 7 T using 30×30 mm^2 FOVs, 1 mm slice thickness, 0.43×0.43 mm^2 in-plane resolutions (70×70 pixels matrix), $G_{acq} = 0.5$ G/cm and $\tau_o = 9$ ms. The fully-refocused 90° chirped SPEN sequence used $T_{exc} = T_{acq} = 21$ ms, $G_{exc} = 0.5$ G/cm, image acquisition in 56 ms; the non-refocused SPEN used $T_{exc} = 4$ ms, $T_{acq} = 21$ ms, $G_{exc} = 2.1$ G/cm. All images were acquired in 50 ms

verifying the reliability of SPEN thermal measurement under these controlled conditions.

SPEN-based thermometry: shift insensitivity and restricted FOV advantages

Among the most important aspects that real-time thermometric methods should present, is immunity *vis-à-vis* shift-driven distortions. Offsets will otherwise affect the ensuing ablation efforts, either via image distortions or by misplacing the regions of interest. Shift effects can in turn involve the presence of fat peaks, field distortions introduced by the ablation transducers and/or ancillary equipment placed in proximity to the patient, or they can even be byproducts of the heating process itself. The SPEN sequences possess a built-in immunity to many of these potential offset artifacts, which will reflect as misplacements Δ (in mm) $= \delta/\gamma G_{exc}$, where δ (in Hz) is the magnitude of the offset. Since this G_{exc} is only marginally related to the resolution or FOVs being sought, this is a feature that can be put to good use towards shift compensation. The consequences of this characteristic can be gauged by considering a thermal change of 50 °C—equivalent to a PRF shift of 0.5 ppm, or ≈150 Hz at 7 T. In typical EPI sequences like the ones hereby used, focusing on a ≈25 mm FOV, 0.35 mm resolution and 0.44 ms echo spacing, this would cause an ≈5-pixel displacement. By contrast in SPEN sequences for which G_{exc} ≈1 G/cm, this PRF-derived shift will be ≈0.025 mm—well under a pixel. This is witnessed by experiments like the one in Fig. 6a, where water in a tube was heated to 75 °C, and EPI/Hybrid SPEN sequences were ran sequentially as the tube cooled to room temperature. The presence of a room-temperature reference allows one to compare the very different thermally-induced shift effects for both cases. A similar phenomenon can be observed in a clinical 3T MRI (Fig. 6b), where a central frequency shift of 200 Hz (half of what would be imparted by the presence of fat) introduces a substsantial voxel displacement in EPI but a nearly negligible one if monitored by SPEN.

Another aspect reflective of this shift insensitivity can be appreciated from the images themselves (Fig. 6a), which not only evidence an overall shift but also larger distortions

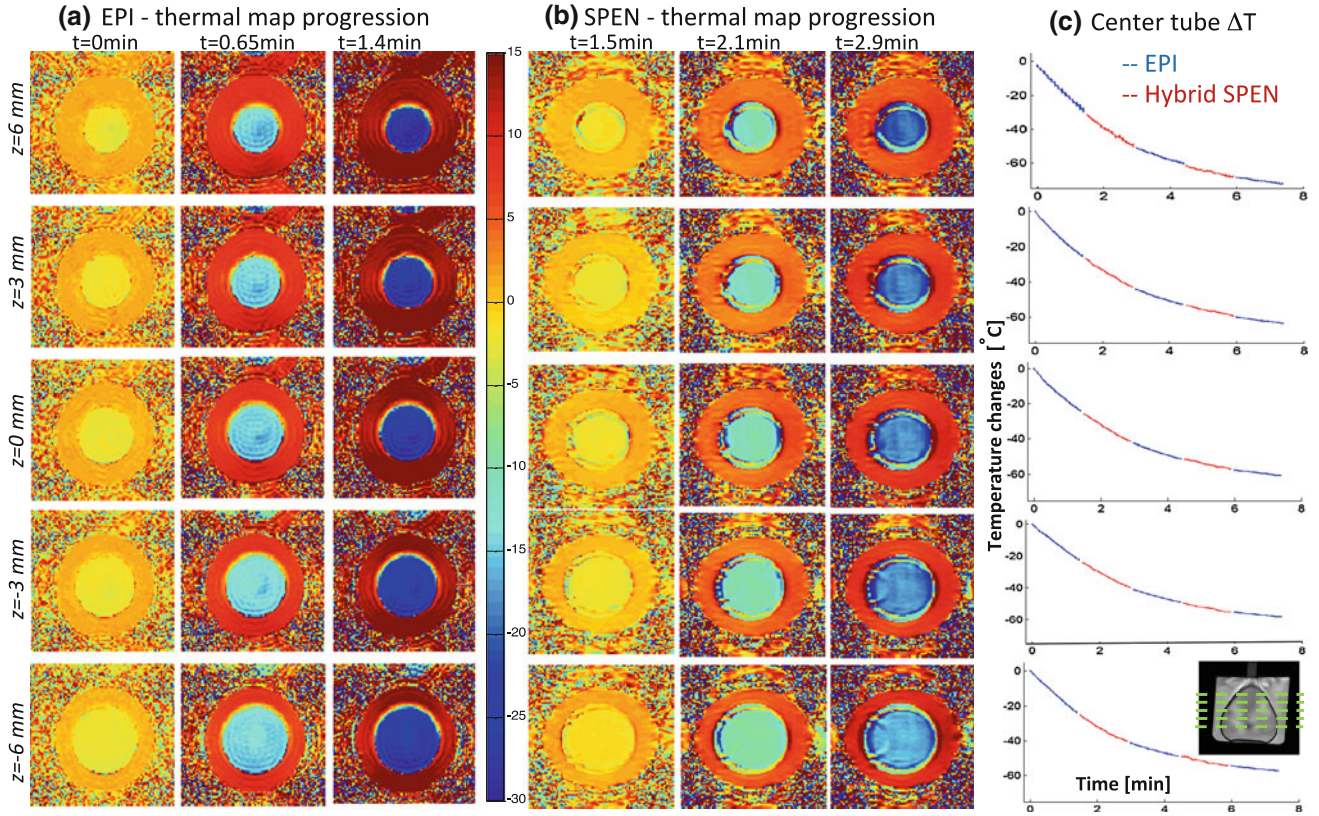

Fig. 5 Comparison between multi-slice EPI and SPEN single-shot results collected at 3 T, on the sample setup shown in the *lower right image*. **a** Thermal EPI maps collected with a TE = 19 ms, showing the progressive cooling of the inner vessel and concomitant heating of the outer one. **b** Thermal maps arising from the SPEN sequence in Fig. 1c. Both (**a**) and (**b**) show the behavior for the same five slices sited at the positions indicated by the *dashed lines* in the *lower right image*, for consecutive acquisitions beginning at the indicated times. Overall fifteen time points were measured for alternating set of experiments, each set with it's own baseline phase map, and temperatures were mapped via PRFs using a $\tau_0 = 19$ ms temperature-related phase accretion. All of the time points acquired are represented in (**c**), which illustrates the average thermal drops evidenced by both methods for the central vessel's cooling. Common acquisition parameters: slice thickness = 3 mm; FOV = 200 × 200 mm^2, resolution = 3.1 × 3.1 mm^2 (64 × 64 pixels matrix), TR = 6 s. SPEN-specific parameters: $T_{acq} = 29.4$ ms; $T_{180} = 14.8$ ms and $G_{180} = 0.47$ G/cm

in the EPI than in the SPEN experiments. This can greatly ease the anatomy tracking that usually accompanies thermometry measurements, and improve its localization attributes. Supplementary Figure A illustrates this more clearly for an instance that mimics the kind of B_0 inhomogeneities that usually accompany ablation devices in close proximity to the targeted tissues.

A final point worth highlighting is SPEN's ability to focus on restricted FOVs. This is a consequence of the method's avoidance of a numerical FT, and thereby of associated folding phenomena. This in turn enables one to "zoom" along the low-bandwidth axis into a particular region of interest, and use a restricted FOV to monitor thermal changes with increased resolution. This can be achieved at no cost in the sequence's complexity (e.g., by the addition of elements like multidimensional RF pulses or outer-volume-suppression procedures) owing to SPEN's reliance on spatially-selective encoding imposing an intrinsic sculpting of the targeted regions. Figure 7 illustrates this for a simple thermometry experiment conducted using two water tubes: a larger one starting with hot water and undergoing cooling, and a smaller one undergoing an inverse, heating process. The goal of the experiment was to zoom in during the thermometry measurement onto the smaller tube, using SPEN's chirped RF pulse ability to selectively excite a FOV of interest in order to improve resolution by a factor 2. The EPI with full-FOV and Hybrid SPEN with half this FOV (and twice the resolution), were run consecutively and temperature profiles inside the tubes were compared. The clear SPEN thermal maps in Fig. 7 summarize the resolution advantages that can result from this capability.

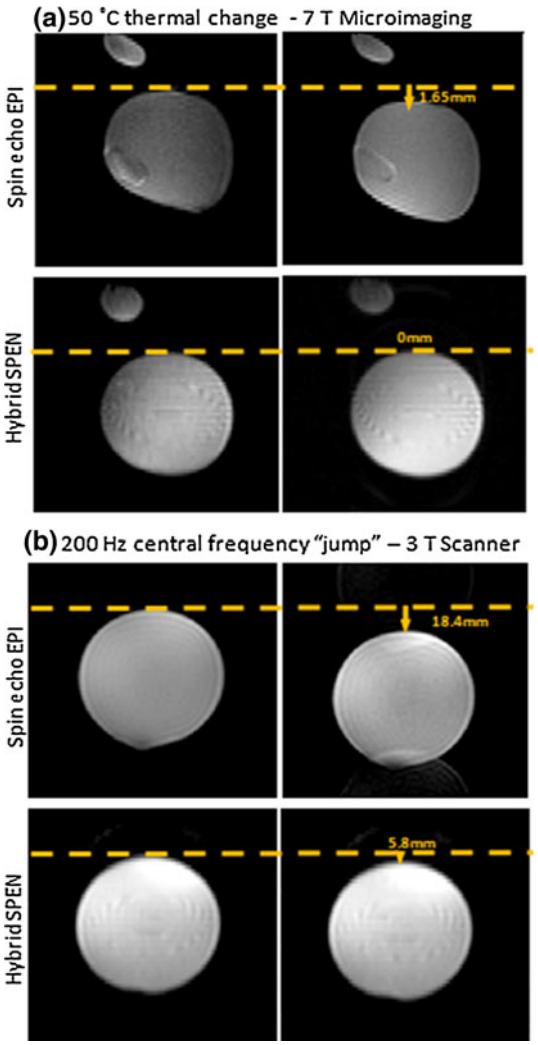

Fig. 6 Comparison between EPI and Hybrid SPEN results arising along the low-bandwidth (*vertical*) dimension under the influence of shift effects. In each instance the *left images* are for referencing; the *right*-hand ones are with the effect. **a** 7 T μimaging thermometry experiments focusing on a larger tube with hot water cooling from 75 °C to room temperature (≈25 °C), and a smaller tube (*top*) that was isolated from the hot one and remained at 25 °C throughout. Common scan parameters: Slice thickness = 2 mm, FOV = 25 × 25 mm^2, resolution 0.36 × 0.36 mm^2 (70 × 70 pixels matrix), T_{acq} = 31 ms; for the 90° chirp SPEN sequence (Fig. 1b) T_{exc} = 26 ms, and G_{exc} = 0.95 G/cm. **b** 3 T whole body scanner MRI results illustrating the spatial displacements caused by a 200 Hz offset in the central frequencies. Other parameters: Slice thickness 5 mm, FOV = 200 × 200 mm^2, resolution 3 × 3 mm^2 (64 × 64 pixels matrix), echo spacing = 0.46 ms, T_{acq} = 30 ms. For the SPEN experiment T_{exc} = 30 ms, G_{exc} = 0.08 G/cm

SPEN-based thermometry: tissue-based examples

Another important issue to validate concerns the relative sensitivity of these experiments, as given by the standard deviations that derive for their measured ΔT. This step of the thermometry verification process was performed on both water and on ex vivo chicken breast specimens. Measurements were performed with no heating or cooling of the scanned object, and standard deviations were calculated over the respective subject areas after subtracting the average temperature from the corresponding thermal maps. Table 2 summarizes representative results stemming from these tests. Worth noting is the higher SNR arising in the Hybrid SPEN cases, upon applying a suitable SR enhancement factor. Once this enhanced sensitivity is achieved, the temperature's STD also drops, showing an expected correlation between the image's SNR and the τ duration as $\frac{\mathrm{std}_{\mathrm{Temp}}^{\mathrm{Hybrid}}}{\mathrm{std}_{\mathrm{Temp}}^{\mathrm{EPI}}} \alpha \frac{\left(\mathrm{SNR}_{\mathrm{Image}}^{\mathrm{EPI}} \cdot \tau^{\mathrm{EPI}}\right)}{\left(\mathrm{SNR}_{\mathrm{Image}}^{\mathrm{Hybrid}} \cdot \tau^{\mathrm{Hybrid}}\right)}$.

A final set of experiments, shown in Fig. 8, demonstrates the ability of fully-refocused SPEN measurements to deliver the magnitude and spatial dependence of temperature changes under in vivo conditions. These changes were imparted with the aid of an air tube carrying gas at differing temperatures, externally attached adjacent to one of the mouse's thighs. The Figure shows temperature maps and profiles for selected locations in the animal's muscle areas, positioned both closer and further away from the heating element. Once again, the Hybrid SPEN image shows a considerably higher faithfulness to the multi-scan reference than its spin-echo EPI counterpart. Due to these images' relatively low SNR, the temperature standard deviations were considerably higher in this animal setup than those measured on the water-based phantoms. Still, similar scatterings are observed between the Hybrid SPEN and the EPI measurements: STD ≈ 2.2 °C for EPI measured over three regions-of-interest, and ≈ 2.0 °C for the Hybrid SPEN results. The time-dependent temperature changes also match well in both sets of measurements, for all locations in the body. Upon considering all three regions analyzed, the average temperature deviations between the EPI and Hybrid SPEN results were ≤0.4 °C.

Discussion and conclusions

This study suggests that SPEN-based imaging can yield comparable –if not superior–thermometric measurements than hitherto available counterparts. SPEN allows one to restrict FOVs to the regions of interest, is largely immune to spatial shifts arising due to thermally-derived central frequency offset shifts, shows only minor distortions in the presence of field inhomogeneities typical of ablation transducers and, in combination with suitable SR reconstruction methods [24], exhibits competitive resolution and sensitivities leading to reduced standard deviations in the temperature measurements. All these

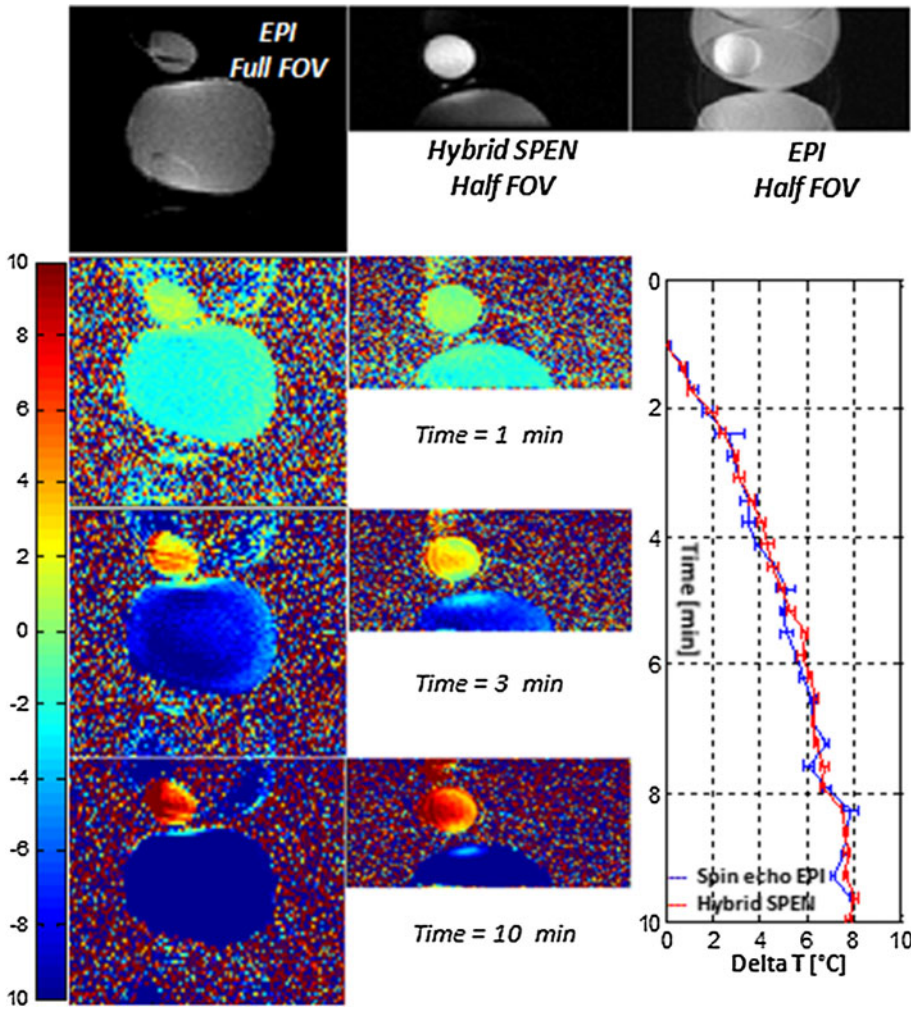

Fig. 7 Thermometry experiment illustrating SPEN's capabilities to zoom into restricted FOVs without suffering from folding artifacts. For all images: slice thickness = 2 mm; FOVs = 25 × 25 mm^2; resolutions = 0.35 × 0.35 mm^2 (70 × 70 pixels matrix), and half-FOVs refer to half these magnitudes along the SPEN axis. In all experiments $\tau_o = 5$ ms, $T_{acq} = 30.8$ ms; for the 90° chirp SPEN sequence $T_{exc} = 26$ ms and $G_{exc} = 0.95$ G/cm. The temperature profiles in the plot reflect averages over a 1 × 1 mm^2 area

Table 2 SNRs and standard deviations (STDs) obtained from spin-echo EPI and fully-refocused SPEN imaging (sequences in Fig. 1a, b)—in the latter case, before and after SR. Common parameters: slice thickness 2 mm, FOV 3 × 3 cm^2, resolution 0.43 × 0.43 mm^2, $\tau_o = 9$ ms

	Water spin-echo EPI	Water hybrid SPEN before/after SR		Ex vivo chicken breast spin-echo EPI	Ex vivo chicken breast hybrid SPEN before/after SR	
SNR	97	87	116	8	13	16
STD (°C)	0.16	0.16	0.14	2.07	1.14	0.91

aspects are important when considering that real-time MR-guided thermometry has to be as immune as possible to distortion effects. Even when carried out in a non-refocused mode, associated to certain disadvantages like spatially-dependent τ-values and hence non-uniform phase accumulations, the SPEN images and their real-time thermometric applications evidence many of these advantages. Particularly promising appear to be the fully-refocused 3D multi-slice sequences of the kind illustrated in Fig. 5, which upon considering the remaining competitive advantages presented by SPEN could result in immediate clinically-oriented applications. It is worth highlighting that additional improvements commonly used to alleviate EPI distortions, like parallel imaging [29, 30], could also be employed to reduce inhomogeneities and accelerate the acquisition of SPEN images [31]. The same can be said if including information from externally measured B_0 maps [19, 32]. Another topic worth of investigation is the possibility of exploiting the intrinsic shift information that SPEN images carry within their measured signals [33, 34]. This could lead to absolute PRF thermometry measurements, without a need to involve additional phase-shift encoding delays τ_o. The potential of these fast 3D, parallel, ΔB_o-compensated, and referenced chemical shift imaging tests, are currently

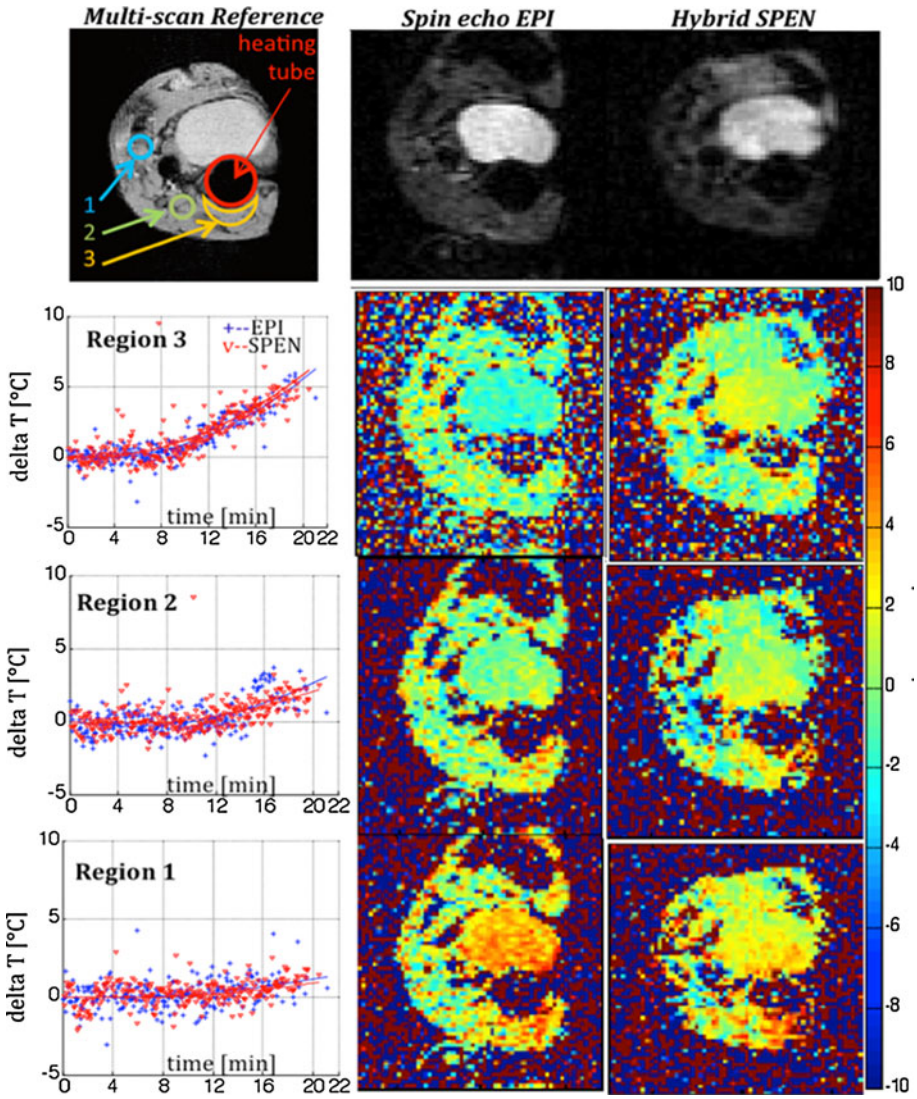

Fig. 8 In vivo mouse images tracking thermal changes in the three indicated muscle areas. (*Top*) Representative 2D multi-scan gradient-echo, spin-echo EPI and fully-refocused SPEN images of the targeted axial slice. The bright object in the center is the animal bladder, the overall blurriness of the single-shot images reflects the challenges arising upon targeting this heterogeneous air/fat/water-containing region at 7 T. (Right-panel color maps, top-to-bottom). Average temperature profiles at *time* = 0, 15, 20 min following the beginning of the heating process. (*Left-panel plots*) Comparisons between the average SPEN-derived (*red*) and EPI-derived (*blue*) temperature maps for the regions indicated as 1, 2 and 3 in the multi-scan reference image. Common scan parameters: slice thickness 1 mm, FOVs = 30 × 30 mm^2, resolution 0.85 × 0.43 mm^2 (35 × 70 pixels matrix), $\tau_o = 4$ ms. For SPEN: sequence in Fig. 1b with $T_{exc} = T_{acq} = 21$ ms, $G_{exc} = 0.3$ G/cm

being explored for thermometric and anatomical applications in challenging regions like liver, intestines, uterus, breast and lungs.

Acknowledgments We are grateful to Dr. Noam Ben-Eliezer for help in the initial stages of this work, and to Koby Zibzener and Talia Harris for their help in setting up the experiments. This research was supported by the Israel Science Foundation (ISF 447/09), the Minerva Foundation (Project 710587; Federal German Ministry for Education and Research), a Helen and Martin Kimmel Award for Innovative Investigation, and the generosity of the Perlman Family Foundation.

References

1. Hindman J (1966) Proton resonance shift of water in the gas and liquid states. J Chem Phys 44:4582–4592
2. Ishihara Y, Calderon A, Watanabe H, Okamoto K, Suzuki Y, Kuroda K, Suzuki Y (1995) A precise and fast temperature mapping using water proton chemical shift. Magn Reson Med 34:814–823
3. Quesson B, de Zwart JA, Moonen CTW (2000) Magnetic resonance temperature imaging for guidance of thermotherapy. Magn Reson Imaging 12:525–533
4. Cline HE, Hynynen K, Hardy CJ, Watkins RD, Schenck JF, Jolesz FA (1994) MR temperature mapping of focused ultrasound surgery. Magn Reson Med 31:628–636
5. Germer C, Isbert CM, Albrecht D, Ritz JP, Schilling A, Roggan A, Wolf KJ, Müller G, Buhr H (1998) Laser thermotherapy for the treatment of liver metastasis. Correlation of gadolinium DTPA-enhanced MRI with histomorphologic findings to determine criteria for follow-up monitoring. Surg Endosc 12:1317–1325
6. Gellermann J, Wlodarczyk W, Hildebrandt B, Ganter H, Nicolau A, Rau B, Tilly W, Fähling H, Nadobny J, Felix R, Wust P (2005) Noninvasive magnetic resonance thermography of recurrent rectal carcinoma in a 1.5 Tesla hybrid system. Cancer Res 65:5872–5880
7. Kuroda K (2005) Non-invasive MR thermography using the water proton chemical shift. Int J Hyperth 21(6):547–560
8. Cernicanu A, Lepetit-Coiffe M, Roland J, Becker CD, Terraz S (2008) Validation of fast MR thermometry at 1.5 T with gradient-echo echo planar imaging sequences: phantom and clinical feasibility studies. NMR Biomed 21:849–858

9. Kickhefel A, Roland J, Weiss C, Schick F (2010) Accuracy of real-time MR temperature mapping in the brain: a comparison of fast sequences. Phys Med 26:192–201
10. Bankson JA, Stafford RJ, Hazle JD (2005) Partially parallel imaging with phase-sensitive data: increased temporal resolution for magnetic resonance temperature imaging. Magn Reson Med 53:658–665
11. Yuan J, Mei C, Madore B, McDannold NJ, Panych LP (2011) Fast fat-suppressed reduced field-of-view temperature mapping using 2DRF excitation pulses. J Magn Reson 210:38–43
12. Holbrook AB, Santos JM, Kaye E, Rieke V, Butts Pauly K (2010) Real-time MR thermometry for monitoring HIFU ablations of the liver. Magn Reson Med 63:365–373
13. Holdsworth SJ, Skare S, Newbould RD, Guzmann R, Blevins NH, Bammer R (2008) Readout-segmented EPI for rapid high resolution diffusion imaging at 3T. Eur J Radiol 65:36–46
14. Roujol S, Ries M, Quesson B, Moonen C, de Senneville BD (2010) Real-time MR-thermometry and dosimetry for interventional guidance on abdominal organs. Magn Reson Med 63:1080–1087
15. Bernstein MA, King KF, Zhou XJ (2004) Handbook of MRI pulse sequences. Academic, Elsevier
16. Kunz D (1986) Use of frequency-modulated radiofrequency pulses in MR imaging experiments. Magn Reson Med 3:377–384
17. Pipe JG (1995) Spatial encoding and reconstruction in MRI with quadratic phase profiles. Magn Reson Med 33:24–33
18. Tal A, Frydman L (2010) Single-scan multidimensional magnetic resonance. Prog Nucl Magn Reson Spectrosc 57:241–292
19. Tal A, Frydman L (2006) Spatial encoding and the acquisition of high definition MR images in inhomogeneous magnetic fields. J Magn Reson 181:179–194
20. Ben-Eliezer N, Shrot Y, Frydman L (2010) High-definition single-scan 2D MRI in inhomogeneous fields using spatial encoding methods. Magn Reson Imaging 28(1):77–86
21. Ben-Eliezer N, Shrot Y, Frydman L (2009) Single-scan spatially encoded MRI—principles & applications. Proc Intl Soc Mag Reson Med 17:2670
22. Goerke U, Garwood M, Ugurbil K (2011) Functional magnetic resonance imaging using RASER. Neuroimage 54(1):350–360
23. Chamberlain R, Park JY, Corum C, Yacoub E, Ugurbil K, Jack CR Jr, Garwood M (2007) RASER: a new ultrafast magnetic resonance imaging method. Magn Reson Med 58(4):794–799
24. Ben-Eliezer N, Irani M, Frydman L (2010) Super-resolved spatially-encoded single-scan 2D MRI. Magn Reson Med 63:1594–1600
25. Ben-Eliezer N, Goerke U, Ugurbil K, Frydman L (2012) Functional MRI using super-resolved spatiotemporally-encoded imaging techniques. Magn Reson Imaging 30:1401–1408
26. Styczynski Snyder AL, Corum C, Moeller S, Powell N, Garwood M (2011) Gradient and frequency modulated excitation for a tailored spatial trajectory with two-dimensional time encoding for Fourier-free imaging. In: Proceedings of the 19th scientific meeting, international society for magnetic resonance in medicine, Quebec, p 4412
27. Ben-Eliezer N, Frydman L (2011) Spatiotemporal encoding as a robust basis for fast three-dimensional in vivo MRI. NMR Biomed 10:1191–1201
28. Rieke V, Butts Pauly K (2008) MR thermometry. Magn Reson Imaging 27(2):376–390
29. Griswold MA, Jakob PM, Heidemann RM, Nittka M, Jellus V, Wang J, Kiefer B, Haase A (2002) Generalized autocalibrating partially parallel acquisitions (GRAPPA). Magn Reson Med 47:1202–1210
30. Heidemann RM, Anwander A, Feiweier T, Knösche TR, Turner R (2012) k-space and q-space: combining ultra-high spatial and angular resolution in diffusion imaging using ZOOPPA at 7 T. NeuroImage 60:967–978
31. Nguyen T, Goerke U, Moeller S, Ugurbil K, and Garwood M (2009) Parallel imaging with RASER using multiband frequency-modulated excitation pulses. In: Proceedings of the 17th scientific meeting, international society for magnetic resonance in medicine, Honolulu, p 2738
32. Jezzard P, Balaban RS (1995) Correcting for geometric distortions in echo planar images from B0 variations. Magn Reson Med 34:65–73
33. Tal A, Frydman L (2007) Spectroscopic imaging from spatially-encoded single-scan multidimensional MRI data. J Magn Reson 189:46–58
34. Schmidt R, Frydman L (2012) In vivo 3D spatial/1D spectral imaging by spatiotemporal encoding: a new single-shot experimental and processing approach. Magn Reson Med. doi: 10.1002/mrm.24470